RSC Applied Polymers

ROYAL SOCIETY OF CHEMISTRY

PAPER

View Article Online
View Journal | View Issue

Cite this: *RSC Appl. Polym.*, 2023, **1**, 315

A unified understanding of magnetorheological elastomers for rapid and extreme stiffness tuning†

Edward J. Barron III, [a,b] Ella T. Williams,[a] Ravi Tutika,[a,b] Nathan Lazarus[c] and Michael D. Bartlett *[a,b]

Magnetorheological elastomers (MREs), which adapt their mechanical properties in response to a magnetic field, can enable changes in stiffness and shape for applications ranging from vibration isolators to shape morphing robots and soft adaptive grippers. Here, a unified design approach is introduced to create MRE materials for extreme stiffness tuning, up to 70×, with rapid (~20 ms) and reversible shape change. This guides the creation of a hybrid MRE composite architecture that incorporates a combination of magnetic particles and magnetic fluids into elastomers. The role of both solid and fluid inclusions on magnetorheological response is systematically investigated and a predictive model is developed that captures the stiffness tuning response of MREs across diverse material microstructures and compositions. This general understanding enables MRE materials with programmable response and greatly enhanced stiffness tuning and rapid response times compared to many MRE, granular jamming, and phase change approaches. This insight is utilized to optimize composites for a soft adaptive gripper which grasps and releases objects of diverse geometries.

Received 13th July 2023,
Accepted 27th September 2023

DOI: 10.1039/d3lp00109a

rsc.li/rscapplpolym

1 Introduction

Adaptive materials which change their stiffness and shape in response to engineering stimuli have emerged as important components for emerging applications such as reconfigurable and adaptive robots and machines.[1–10] One essential feature of these materials is the ability to rapidly undergo extreme changes in stiffness to enable multifunctional components. Stiffness tuning can be accomplished at the material level by utilizing mechanisms such as phase change,[11–13] granular jamming,[14–16] or magnetic material response.[17,18] The stiffness tuning capability of a material is typically an experimentally measured quantity for several performance parameters including the magnitude of stiffness, the stiffness tuning ratio, and the response time.[19] For example, materials utilizing low melting point alloys and polymers have demonstrated large changes in stiffness by taking advantage of their solid–liquid phase transition in response to heat.[4,11,13,20] Granular media rapidly responds to negative pressure with a transition between a fluid-like granular state, where particles freely move past each other, to a jammed state, where the jammed particles form a solid-like mechanical response.[14–16,21] Magnetically active materials such as magnetorheological elastomers (MREs) have some of the fastest response times among stiffness tuning materials (<0.01 s),[22,23] however, the stiffness change of traditional MRE systems (~10×) is typically lower than that of other stiffness tuning materials.[22,24] Improvement of the stiffness tuning effect of MREs offers the possibility to create adaptive materials with both rapid response and extreme stiffness tuning that enable the next generation of adaptive machines.

Magnetic elastomer composites have traditionally been created by incorporating magnetic particles into soft elastomers such as silicones or polyurethanes,[25] to provide a combination of soft mechanical response and magnetic functionality for applications including stretchable and adaptive electronics and sensing,[26–31] automotive components,[32–34] and soft robotic grippers.[35–39] A key feature that has lead to substantial research of MREs is their magnetorheological effect, which leads to magnetic field-driven tunable stiffness,[17,18] variable energy dissipation and damping,[40,41] and shape-memory effects.[42] To improve the stiffness tuning effect (often called the MR effect or MR ratio) of these materials, MREs have been created with varied parameters such as elastomer matrix material,[43–50] magnetic particle size,[28,43,48,51] shape,[52–54] and volume fraction,[44,55–57] and recently through the introduction of magnetic fluids as functional content.[29,42,58] Magnetorheological fluids, which are magnetic fluids that

[a]*Mechanical Engineering, Soft Materials and Structures Lab, Virginia Tech, Blacksburg, VA 24061, USA. E-mail: mbartlett@vt.edu*
[b]*Macromolecules Innovation Institute, Virginia Tech, Blacksburg, VA 24061, USA*
[c]*Electrical and Computer Engineering Department, University of Delaware, Newark, DE 19716, USA*

† Electronic supplementary information (ESI) available. See DOI: https://doi.org/10.1039/d3lp00109a

rapidly change viscosity and yield stress when subjected to a magnetic field,[59,60] have recently been used as inclusions for MREs. These fluid inclusions are incorporated as millimeter-scale droplets into elastomers through 3D printing or by micro-dispersing magnetorheological fluid droplets through mixing, and provide unique opportunities to achieve large stiffness tuning with highly deformable and adaptive properties.[29,42,58,61] However, how stiffness tuning and response in these diverse MREs depends on material composition and microstructure is not well understood, which limits performance and programming of desired properties.

Here we determine a predictive model for the understanding and enhancement of MRE properties to optimize magnetic elastomers with rapid material response and extreme stiffness tuning. The model is validated through MREs with diverse material architectures, which includes traditional rigid particle composites (RCs), state-of-the-art magnetorheological fluid composites (FCs), and a new form of hybrid composite (HC) MRE which contains both rigid particles and magnetorheological fluids as discrete domains (Fig. 1a–c). We systematically investigate the effects of material structure and zero-field mechanical response on the MR effect of MREs, and find that our model unifies the stiffness tuning effect for each of the three investigated microstructures under a single predictive equation (Fig. 1d). This quantitative understanding of the relationship between zero-field modulus and MR effect allows for the optimization of MRE performance, which we show through the creation of MRE materials with unprecedented changes in stiffness (70×) (Fig. 1e) and rapid magnetic response times of ~20 ms (Fig. S1†) (Movie S1†). The magnetorheological response of these materials gives rise to a rapidly reversible shape-locking and stiffness tuning effect (Fig. 1f), which we utilize through our multi-phase HC MRE (Fig. 1g) to create adaptive grippers for controlled manipulation of diverse objects.

2 Results and discussion

2.1 Predicting MRE stiffness tuning

To predict the stiffness tuning of magnetically active composite materials, we consider a material effect from the composite zero-field modulus ($E_{c,B=0}$) and a magnetic contribution (E_{mag}). When subjected to a magnetic field, we assume that the material and magnetic forces are additive (*i.e.* a parallel arrangement of springs) which yields a composite modulus, E_c, such that $E_c = E_{c,B=0} + E_{mag}$. We then normalize this equation by $E_{c,B=0}$ to understand how the tunability of the magnetic composite depends upon both the material contribution and the effective magnetic contribution:

$$\frac{E_c}{E_{c,B=0}} = E_{mag}{E_{c,B=0}}^{-1} + 1 \quad (1)$$

Eqn (1) gives an analytical expression for the MR enhancement factor $\left(\frac{E_c}{E_{c,B=0}}\right)$, which is the ratio between the composite modulus under a magnetic field (*i.e.* activated) and the zero-field modulus of the composite (*i.e.* unactivated), where large values indicate high stiffness tunability. When the MR enhancement factor approaches a value of 1, the composite modulus does not increase when subjected to a magnetic field, which occurs as $E_{mag} \ll E_{c,B=0}$. This provides a lower, physical limit to rigidity tuning when magnetic interactions are low or when the initial composite modulus is high. Eqn (1) provides a clear design paradigm where maximum rigidity tuning is achieved when magnetic interactions are increased or when initial composite modulus is lowered. From a materials design perspective, this requires an approach to achieve significant magnetic material loading to increase the magnetic effect, while still maintaining a soft composite response. Through this general guidance, we will show how composite microstructure and composition can be used to achieve high degrees of stiffness tuning and programmable composite modulus.

We can also rearrange this relationship to predict a parameter that is commonly used to quantify stiffness tuning for MREs: the MR effect (MR_{effect}), or the relative change in modulus of the sample. By utilizing the relationship between parallel springs and solving for MR_{effect}, the MR effect can be modeled as a function of $E_{c,B=0}$ and E_{mag}:

$$MR_{effect} = E_{mag}{E_{c,B=0}}^{-1} \times 100\% \quad (2)$$

These simple yet robust relationships provide an accurate fit to the data acquired in this work across RC, FC, and HC composite architectures over several orders of magnitude in zero-field modulus of the composites, where E_{mag} is used as a fitting parameter (Fig. 1d). We consider $E_{c,B=0}$ a primary factor in determining the magnetorheological response, as previous work has shown that stiffness tuning becomes limited as the zero-field modulus of the composite increases.[62] This is consistent with our results and prediction, where $MR_{effect} \propto {E_{c,B=0}}^{-1}$, demonstrating that as $E_{c,B=0}$ increases MR_{effect} decreases.

We note that eqn (1) and (2) are not simply the equations for the MR effect, which is typically an experimentally measured quantity relating the modulus of the material under a magnetic field (E_c) relative to the same material without a magnetic field ($E_{c,B=0}$), *i.e.* $\left(\frac{E_c - E_{c,B=0}}{E_{c,B=0}} \times 100\%\right)$. Eqn (1) and (2) instead give insight into the stiffness tuning contributions from the inherent stiffness of the composite material ($E_{c,B=0}$) and the effective stiffness imparted to the material through an applied magnetic field (E_{mag}).

2.2 MRE composition

To determine the effect of microstructure on the magnetorheological response, as guided by eqn (1) and (2), we fabricate MREs of three different material architectures and mechanically quantify their stiffness tuning properties. RC MREs are fabricated with a volume fraction of 25% iron powder within the elastomer matrix. This volume fraction was chosen as it

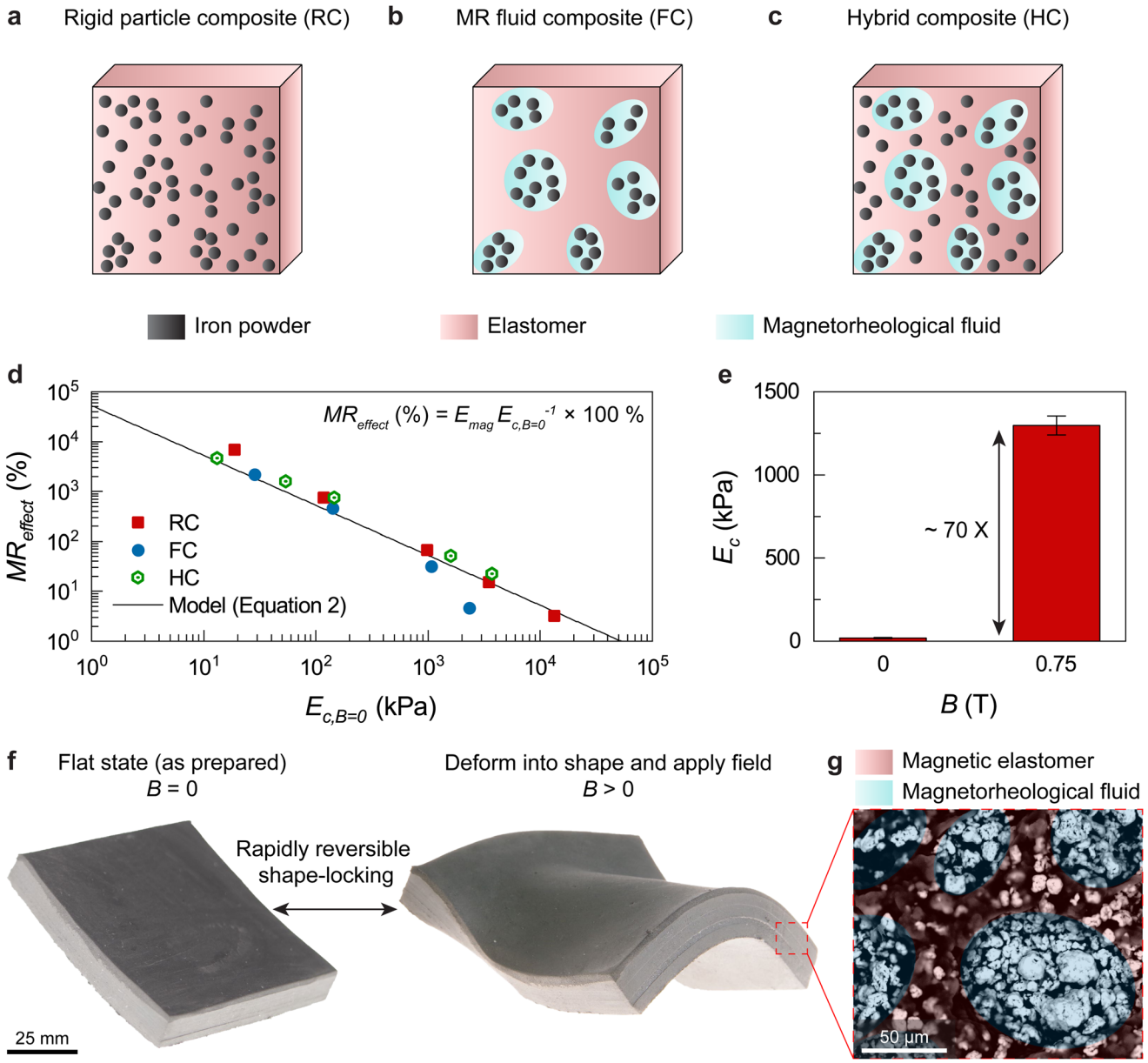

Fig. 1 Material structure and properties. (a) Schematics of rigid particle composite (RC), (b) magnetorheological fluid composite (FC), and (c) hybid composite (HC) material architectures. (d) Effect of zero-field modulus on the relative MR effect of the materials tested in this work (E_{mag} = 530 kPa for eqn (2)). (e) Change in stiffness of an RC MRE with no field applied and with a magnetic flux density of 0.75 T. (f) Image of a hybrid composite magnetorheological elastomer utilizing magnetorheological stiffness tuning to realize a shape memory effect. (g) SEM image of hybrid composite MRE. The image is artificially colored red for the magnetic elastomer phase and blue for the MR fluid phase. An unaltered image can be found in Fig. S2.†

allowed for a low enough viscosity to be easily processed into testing geometries, while also imparting a significant magnetic response. FC MREs incorporate an iron based MRF that contains a volume fraction of 35% iron powder in a propylene glycol carrier fluid that is immiscible with the silicone matrix and processed to be contained as discrete microdroplets within the elastomer. The volume fraction of MRF in the FC MREs is 50%, leading to a total iron powder volume fraction of 17.5%. Above an MRF volume fraction of 50% large-scale phase separation occurred and evenly dispersing the MRF as microdroplets was a challenge. This volume fraction of MRF is higher than that reported in previous work for FC MREs which showed MRF volume fractions of 30–40%.[42,61] HC MREs are fabricated with a volume fraction of 50% MRF, as well as 15% iron powder located in the elastomer matrix for a total iron particle volume fraction of 25%, which is equivalent to the volume fraction of magnetic content in the RC MREs. Scanning electron microscopy of the RC, FC, and HC material architectures can be found in Fig. S3 and S4.† In addition to investigating microstructure, the elastic modulus of the sili-

cone matrix (E_m) is varied to study the effect of zero-field modulus on the stiffness tuning capabilities for each of the MRE material architectures. E_m is controlled by changing the crosslinking density of the silicone matrix, or by creating blends of two silicone elastomers with different matrix moduli (details in the Experimental section).

2.3 MRE characterization

The MR effect of the magnetic elastomer composites is measured through a custom magnetorheological compression fixture (Fig. 2a). The MRE testing fixture consists of a copper electromagnetic coil integrated with a 1020 steel bottom compression plate and an outer steel housing (top compression plate). Compression tests are run on each material using the electromagnet with average magnetic field strengths of H = 0–280 kA m^{-1}. Finite element analysis (FEA) is used to determine the average magnetic flux density through the samples (Fig. 2b), which is determined to be up to 0.75 T for the RC and HC MREs and up to 0.58 T for the FC MREs (Fig. S5†). The difference in flux density arises from the difference in magnetic content between the material architectures.

Representative compression curves for RC, FC and HC MREs with constant E_m = 200 kPa are shown in Fig. 2c–e respectively, with the solid lines representing the zero-field mechanical response and the dashed lines indicating the mechanical response with an applied field of 280 kA m^{-1}. For the same matrix modulus, RC MREs demonstrate a more rigid zero-field mechanical response than the FC and HC MREs. This is attributed to the incorporation of MRF in both the FC and HC MREs, which mechanically cloaks the rigid character of the solid particle inclusions and creates a softer composite mechanical response. The RC MRE also shows a substantially smaller change in mechanical properties under the influence of a 280 kA m^{-1} field. From our understanding introduced in Fig. 1d we attribute this to the larger zero-field modulus of the RC MREs. Thus, to program the magnitude of the magnetorheological stiffness effect, it becomes necessary to control the zero-field modulus of the composite ($E_{c,B=0}$).

Control over $E_{c,B=0}$ is demonstrated through two material design strategies: the microstructure of the MREs can be changed to either increase or decrease the modulus of the composite by utilizing rigid particle or MRF inclusions, or E_m can be varied through changes in elastomer crosslinking which has a strong influence on the composite modulus. These two design strategies allow for diversity of fabrication in the event that an application is limited by either the choice of elastomer or the magnetic inclusions. Fig. 2f shows the change in zero-field modulus with respect to each of the material architectures with a constant E_m of 200 kPa. The compressive moduli are determined from the linear portion of the of the stress *versus* strain curves (details in Experimental). The addition of solid filler increases the zero-field modulus of the composite, while the addition of the MRF decreases the modulus of the composite. Fig. 2g shows the alternative method of controlling the zero-field modulus for a constant material architecture of HC MRE by varying the elastomer modulus, E_m. Controlling the zero-field modulus of the composite by either of these two methods has a strong influence on the magnetorheological effect.

2.4 Active magnetorheological properties

For MREs to be utilized for active property tuning, it is essential to understand how the MRE material properties relate to the active stiffness tuning response. We determine that the zero-field modulus, $E_{c,B=0}$, is the controlling factor in determining the stiffness tuning capabilities of MREs. Fig. 3a shows the range of achievable modulus of MREs as a function of zero-field modulus. The lowest point on each bar represents the lowest achievable modulus ($E_{c,B=0}$) of the sample, while the highest point of each bar is the modulus under an applied field of H = 280 kA m^{-1}. The softest MREs in this work were fabricated with $E_{c,B=0}$ on the order of 10 kPa, and demonstrate changes of stiffness of up to 70× their zero-field modulus. As the zero-field modulus is increased up to 13 MPa the relative tunability of the composite modulus decreases to only ~3%. This decrease in mechanical tunability with respect to $E_{c,B=0}$ is a fundamental trade-off in these material systems that is attributed to stiffer material resisting the distortion of the composite by the magnetic inclusions,[62,63] creating a large effect of $E_{c,B=0}$ relative to E_{mag}.

Fig. 3b shows the maximum measured MR enhancement factor as a function of $E_{c,B=0}$ for the materials tested in this work as well as literature data.[17,24,42,56,57] Here, we focus only on the maximum achievable stiffness tuning effect to understand the factors governing the creation of extreme stiffness tuning MREs. We find that eqn (1) accurately predicts the stiffness tuning effect of not only the MREs in this work, but of those reported in previous research as well by fitting the data to a single value of E_{mag}. The data is fit with a value of E_{mag} = 530 kPa, which remains accurate across the wide range of $E_{c,B=0}$, is independent of the investigated microstructures, and fits a wide variety of iron particle volume fractions ranging from 17–30%, and MRF volume fractions from 40–50%. The MR enhancement factor is shown to approach a value of 1, indicating a negligible change in modulus as $E_{c,B=0}$ is increased above 1 MPa, which quantifies the fundamental tradeoff between MRE active properties and their zero-field modulus. This is consistent with the prediction that when $E_{mag} \ll E_{c,B=0}$ the MR enhancement factor approaches 1. This finding is an essential result for the optimization of MREs, in that it provides evidence that the maximum magnetic contribution to the modulus is not drastically changed by any of the three material structures. E_{mag} is instead likely primarily a factor of the magnetic properties of the inclusions, where iron is most commonly chosen because of its high permeability, high saturation, and low remnant magnetization.[50,64]

For materials with the same magnetic inclusions, the ability to tune E_{mag}, even across relatively large changes in volume fraction, does not have as great of an effect on the maximum stiffness tuning effect as $E_{c,B=0}$. By understanding that zero-field modulus is a dominant factor in determining the stiffness tunability of these material systems, we can now

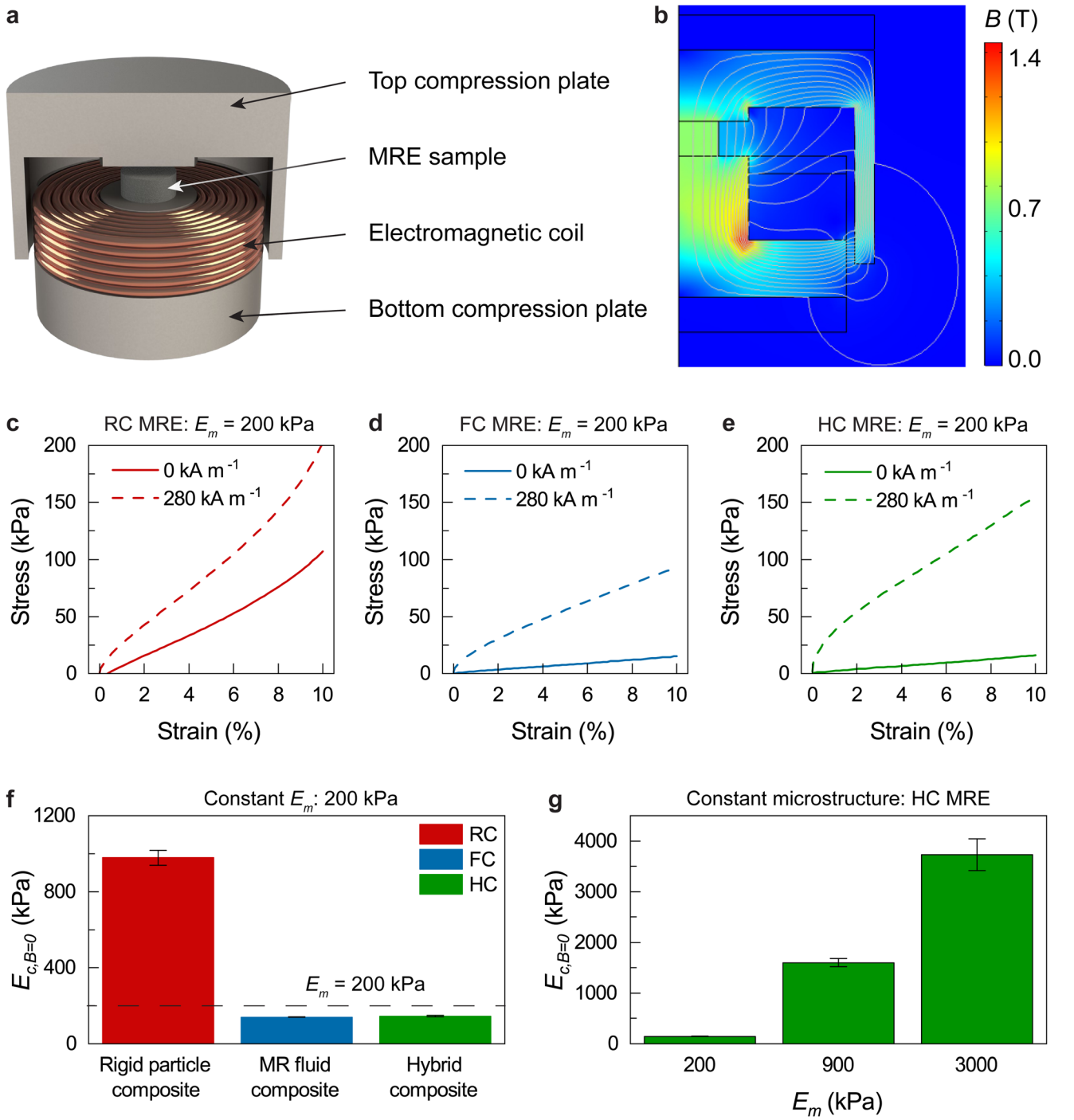

Fig. 2 Magnetorheological elastomer characterization. (a) Schematic of the magnetic compression fixture used to determine magnetorheological properties in this work. (b) FEA analysis for RC and HC MREs to determine the magnetic flux density and uniformity throughout the compression specimen. (c) Compressive stress–strain curves of Ecoflex RC, (d) FC, and (e) HC MRE with 0 and 280 kA m^{-1} applied fields. (f) Tunability of zero-field modulus with respect to material architecture for constant elastomer matrix modulus. (g) Tunability of zero-field modulus with respect to matrix modulus with constant material architecture.

program the MR effect through their zero-field response by utilizing either E_m or material structure as discussed in Fig. 2f and g.

MREs have long been known to have rapid response times, however the stiffness tunability has been lacking when compared to other active material systems.[22] By creating MREs with a sufficiently low zero-field modulus, we can produce materials with extreme stiffness tuning effects (MR_{effect} = 7000%) that are greater than many granular jamming and low melting point systems,[3,11,13,21] while showing faster response

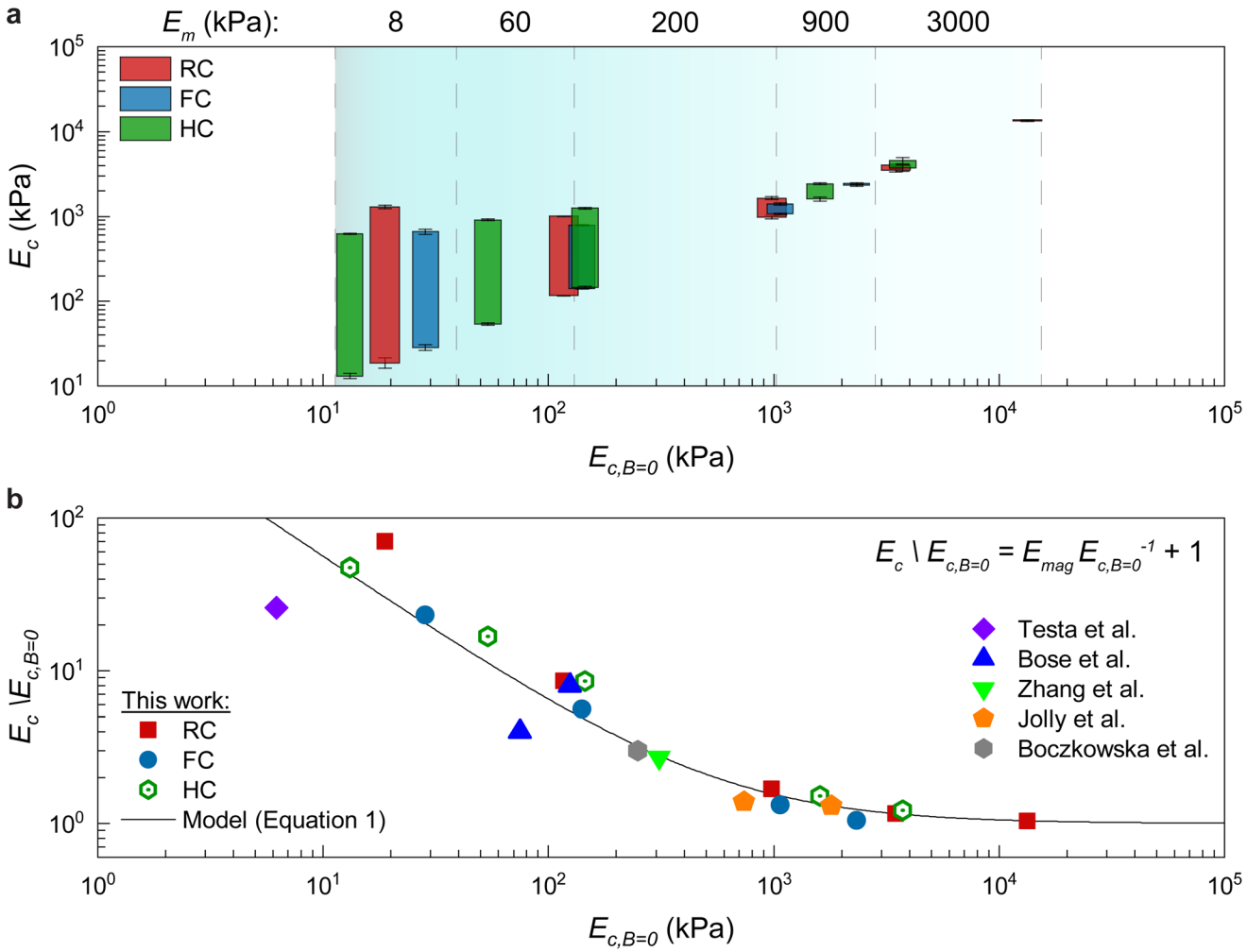

Fig. 3 Magnetorheological stiffness tuning. (a) Range of achievable moduli of MREs as a function of their zero-field modulus. The bottom of the floating bars indicate the zero-field modulus of the sample, while the top of the bars correspond to the measured modulus with an applied field of 280 kA m^{-1}. (b) Maximum measured magnetorheological enhancement ratio as a function of zero-field modulus for the materials tested in this work as well as literature data (E_{mag} = 530 kPa for eqn (1)).[17,24,42,56,57]

times on the order of ~20 ms. The results of this work produce a clear design framework for MREs of diverse structures that allows for the optimization of MRE materials with extreme stiffness tuning capabilities and rapid response, overcoming trade-offs in MRE and phase change based stiffness tuning materials.

2.5 Adaptive MRE gripper

The magnetorheological response of the HC MREs leads to a shape-locking effect with a rapid material response to a magnetic field. Here we show a soft adaptive gripper capable of rapidly gripping and releasing delicate and rigid objects with diverse geometries (Fig. 4 and Movie S2†). The gripper consists of an HC MRE (E_m = 200 kPa) membrane which becomes rigid and locked into shape through a magnetic field, integrated with an inflated air pocket which allows for rapid reversibility to drop the object upon reduction of the field. The MRE gripper is adhered to the center of the electromagnet (Fig. 4a), where the magnetic field is controlled electronically.

The gripper is able to passively conform around delicate objects without damage, and then grasp upon the application of an applied magnetic field, which increases the stiffness of the MRE membrane and locks in the conformed shape. Fig. 4b demonstrates the grasping of a tomato, where (i) the gripper begins to approach the object, (ii) the gripper conforms around the object and the magnetic field is applied, (iii) the gripper is retracted while grasping the object, and (iv) after holding the object for 10 seconds at its original position, the magnetic field is turned off and the object rapidly drops from the gripper in less than 0.07 s. The adaptive gripper is also able to adapt to objects of complex geometry, which is shown through the grasping of a lego brick (Fig. 4c), objects of small cross-sectional area such as a marker (Fig. 4d), and complex, multipart shapes such as a cluster of grapes (Fig. 4e). This HC MRE composite gripper is enabling for areas such as robotic

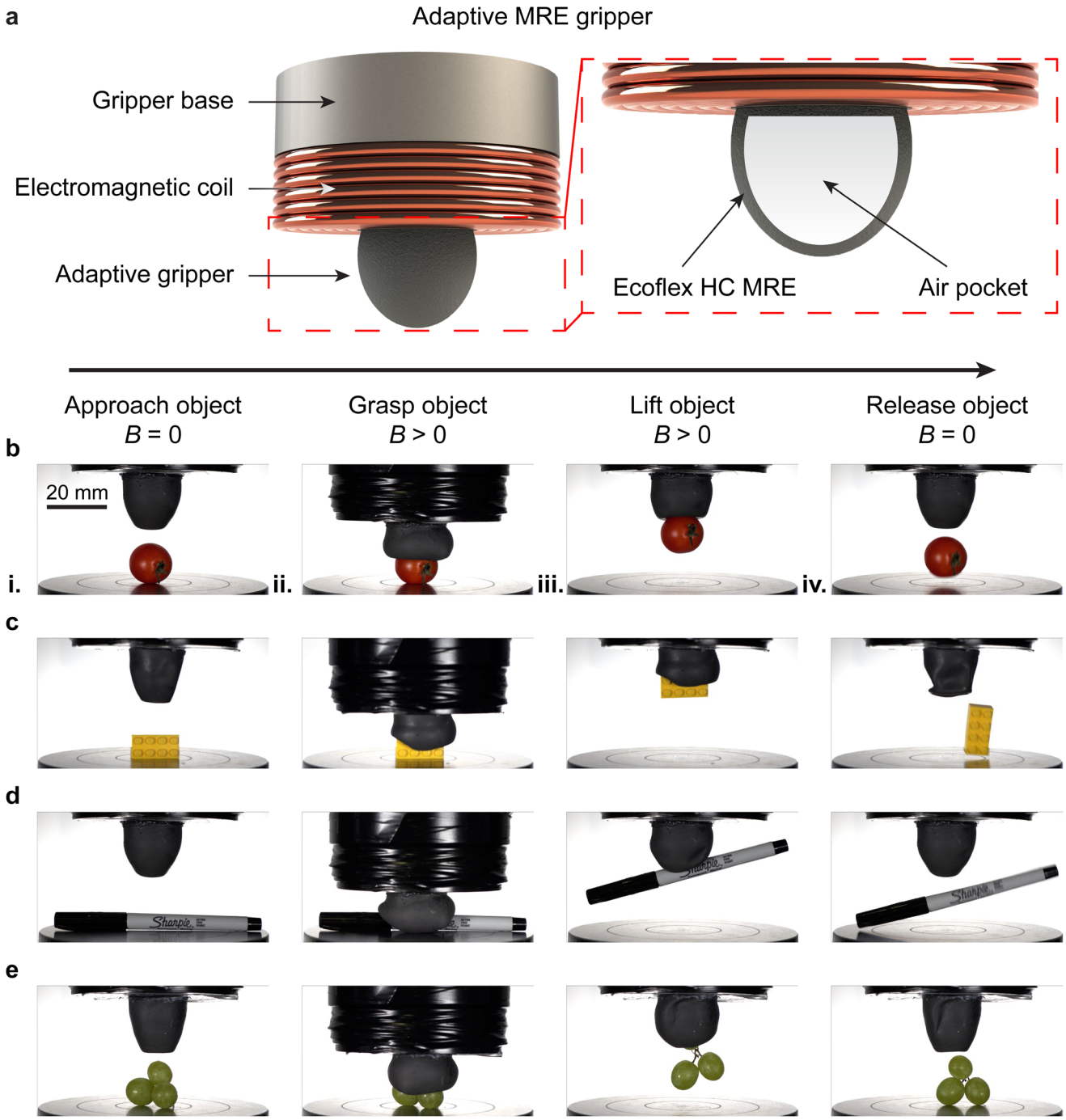

Fig. 4 Adaptive MRE gripper. (a) Schematic of an adaptive gripper consisting of an HC MRE membrane and an incorporated air pocket and test fixture. (b) Images of the adaptive gripper grasping a tomato, (c) a lego brick, (d) a marker, and (e) a cluster of grapes.

manipulation and manufacturing which may require diverse grasping capabilities.

3 Conclusion

A unified MRE stiffness tuning model is demonstrated which accurately predicts the stiffness tuning effect of diverse MRE architectures. As a result of this model, the fundamental tradeoff between MR effect and zero field modulus is quantified, and materials above $E_{c,B=0}$ = 1 MPa are shown to have a drastically reduced MR enhancement factor approaching 1. This fundamental understanding of MRE active properties is utilized to create MREs with unprecedented MR effects of up to 7000% that can respond on the order of 20 ms. The large mechanical adaptability and rapid response of the MREs

shown in this work are expected to have applicability towards stiffness tuning elements for applications in robotics, transportation, and active technologies such as human–machine interfaces. Further, the improved understanding of the microstructure and magnetorheological response of soft composites is expected to have impacts on the development of active and programmable material systems for future advancements in functionality.

4 Experimental section

4.1 Silicone elastomer fabrication and mechanical property control

The silicone elastomers in this work utilize Sylgard 184 poly (dimethylsiloxane) (PDMS) silicone elastomer (Dow Silicones) which is a two part silicone elastomer, Ecoflex 00-30 (Smooth-On) which is a two-part platinum-catalyzed silicone elastomer, or a combination of the two silicone elastomers to vary E_m. The elastomers are prepared prior to the introduction of magnetic content. The silicone matrix with E_m = 8 kPa is made utilizing PDMS. The PDMS is mixed with a 60 : 1 ratio of base to curing agent in a dual asymmetric centrifugal (DAC) mixer under vacuum (FlackTek) at 1800 rpm for 100 s. For the silicone with E_m = 60 kPa, the PDMS is mixed with a 45 : 1 ratio of base to curing agent at 1800 rpm for 100 s under vacuum. The silicone matrix with E_m = 200 kPa is made utilizing Ecoflex 00-30. Ecoflex is mixed with equal parts by weight of part A and part B. The uncured elastomer is mixed for 270 s at 2000 rpm under a vacuum. The silicone matrix with E_m = 900 kPa is made utilizing a combination of PDMS and Ecoflex 00-30. Ecoflex is mixed with equal parts by weight of part A and part B for 270 s at 2000 rpm under a vacuum. PDMS is mixed with a 10 : 1 ratio of base to curing agent at 1800 rpm for 100 s. The two uncured elastomers are combined in a 1 to 1 ratio by weight. The mixture is then mixed for 270 s at 2000 rpm under a vacuum. The silicone matrix with E_m = 3000 kPa is made utilizing PDMS. The PDMS is mixed with a 10 : 1 ratio of base to curing agent at 1800 rpm for 100 s under vacuum. Further information about the composition of these silicones can be found in Table S1.†

4.2 Composite fabrication

RC MREs are fabricated with iron powder (mean particle diameter: 5 μm, US Research Nanomaterials) with a particle volume fraction of $\Omega_{composite}$ = 25%. A 35% volume fraction of iron powder in propylene glycol is used to create the MRF used for both the FC and HC MREs (Ω_{MRF} = 35%). FC MREs are fabricated with an MRF volume fraction of Ψ = 50%. The HC MRE consists of an MRF volume fraction Ψ = 50% and a magnetic elastomer phase with Ω_{matrix} = 15%. The total iron powder volume fraction for FC and HC MREs can be determined by $\Omega_{composite,FC} = \Psi\Omega_{MRF}$ and $\Omega_{composite,HC} = \Psi\Omega_{MRF} + (1 - \Psi)\Omega_{matrix}$, giving values of $\Omega_{composite,FC}$ = 17.5% and $\Omega_{composite,HC}$ = 25% respectively. Further information about the composition of these materials can be found in Table S2.†

RC MREs are fabricated by adding the 25% by volume iron powder to the uncured silicone elastomer and then mixing at 800 rpm for 120 s under vacuum in a FlackTek SpeedMixer. The molded samples were then cured in a convection oven for at least 12 hours at 40 °C.

FC MREs are fabricated by adding the magneteorhelogical fluid to the uncured elastomer in a 50% mixture by volume. The composite is then mixed for 120 s at 800 rpm under vacuum in the SpeedMixer. The samples are cured by convection oven for at least 12 hours at 40 °C.

HC MREs are fabricated by adding 15% iron powder by volume to the uncured elastomer. Hexanes are added in a 1 : 4 proportion to the uncured elastomer by weight to reduce the viscosity for ease-of-processing. The composite is then mixed for 120 s at 800 rpm at atmospheric pressure in the SpeedMixer. The magnetorheological fluid is then added to the mixture in a 1 : 1 ratio of MRF to elastomer and iron powder by volume. The mixture is then hand mixed. The material is poured into molds, placed under vacuum to remove residual hexanes, then cured for at least 12 hours in a convection oven at 40 °C.

4.3 Magnetorheological testing fixture

A two part magnetic compression testing fixture was machined out of 1020 steel. The bottom half of the fixture is a compression plate, and the top half is a steel housing to increase the magnetic flux density through the material. 500 turns of 18 AWG copper of wire are integrated with the bottom compression plate to provide the magnetic field. Currents of 0–7 A are supplied to the electromagnet resulting in average magnetic field strengths of H = 0–280 kA m^{-1}.

4.4 Magnetorheological compression tests

Compression samples were cured in 28.6 mm diameter, 12.5 mm deep molds. Samples are tested *via* a multi-step process with the MRE loaded in the magnetic compression testing fixture. Because the test fixture itself is subject to a force when a magnetic field is applied to the system, a series of reference tests are used to determine what proportion of the measured load was applied as a stress to the sample. First, reference data is taken by measuring the load exerted by the magnetic field on the sample at several static displacements and all applied currents. A power law curve is fit to the reference data for each sample to model the load exerted by the magnetic field during sample testing. Compression tests with three loading and unloading cycles are then carried out on the sample with currents from 0–7 A applied to the electromagnet. The load from the power law model is then subtracted from the compression test load data to determine the material response to the magnetic field. Tests were performed at a rate of 12 mm min^{-1} and the compressive modulus was calculated by determining the slope of a linear fit of the stress *versus* strain data from 2.5–7.5% strain.

4.5 Adaptive gripper fabrication

The gripper is made from an HC MRE (E_m = 200 kPa) cast into a 30 mL high form crucible. The uncured composite is placed under vacuum to remove residual hexanes. The material is then poured into the crucible and then checked for air inclusions. Then, the bulk of the material is poured out leaving a thin coating (similarly to a slipcasting process). The crucible is then immediately set upside down on the glass plate, which allows the excess material to flow down onto the plate creating a sealed bottom. The mold is then placed in a 40 °C oven and allowed to fully cure for at least 45 min.

Author contributions

E. J. B., E. T. W., N. L., and M. D. B. designed research; E. J. B., E. T. W., and R. T. performed research; E. J. B., E. T. W., N. L., and M. D. B. analyzed data; E. J. B., E. T. W., N. L., and M. D. B. wrote the paper.

Conflicts of interest

There are no conflicts to declare.

Acknowledgements

We acknowledge support from the Office of Naval Research Young Investigator Program (YIP) (N000142112699) and by the Army Research Laboratory under cooperative agreement number W911NF-20-2-0039. The views and conclusions contained in this document are those of the authors and should not be interpreted as representing the official policies, either expressed or implied, of the Army Research Laboratory or the U.S. Government. The U.S. Government is authorized to reproduce and distribute reprints for Government purposes notwithstanding any copyright notation herein. This work was performed in part at the Nanoscale Characterization and Fabrication Laboratory, which is supported by the Virginia Tech National Center for Earth and Environmental Nanotechnology Infrastructure (NanoEarth), a member of the National Nanotechnology Coordinated Infrastructure (NNCI), supported by NSF (ECCS 1542100 and ECCS 2025151).

References

1 A. Mohammadi Nasab, S. Sharifi, S. Chen, Y. Jiao and W. Shan, *Adv. Intell. Syst.*, 2021, **3**, 2000166.
2 M. A. Karimi, V. Alizadehyazdi, B.-P. Busque, H. M. Jaeger and M. Spenko, 2020 3rd IEEE International Conference on Soft Robotics (RoboSoft), 2020, pp. 291–296.
3 Y. Jiang, D. Chen, C. Liu and J. Li, *Soft Rob.*, 2019, **6**, 118–132.
4 D. Hwang, E. J. Barron III, A. T. Haque and M. D. Bartlett, *Sci. Rob.*, 2022, **7**, eabg2171.
5 J. W. Boley, W. M. Van Rees, C. Lissandrello, M. N. Horenstein, R. L. Truby, A. Kotikian, J. A. Lewis and L. Mahadevan, *Proc. Natl. Acad. Sci. U. S. A.*, 2019, **116**, 20856–20862.
6 A. L. Evenchik, A. Q. Kane, E. Oh and R. L. Truby, *Annu. Rev. Mater. Res.*, 2023, **53**, 225–251.
7 T. Amadeo, D. Van Lewen, T. Janke, T. Ranzani, A. Devaiah, U. Upadhyay and S. Russo, *Front. Robot. AI*, 2022, **8**, 731010.
8 Y. Kim, H. Yuk, R. Zhao, S. A. Chester and X. Zhao, *Nature*, 2018, **558**, 274–279.
9 Z. Xu, R. Hensleigh, N. J. Gerard, H. Cui, M. Oudich, W. Chen, Y. Jing and X. R. Zheng, *Addit. Manuf.*, 2021, **47**, 102321.
10 L. T. Gaeta, K. J. McDonald, L. Kinnicutt, M. Le, S. Wilkinson-Flicker, Y. Jiang, T. Atakuru, E. Samur and T. Ranzani, *Soft Matter*, 2023, **19**, 2623–2636.
11 H. Dong and G. M. Walker, *Smart Mater. Struct.*, 2012, **21**, 042001.
12 T. L. Buckner, M. C. Yuen, S. Y. Kim and R. Kramer-Bottiglio, *Adv. Funct. Mater.*, 2019, **29**, 1903368.
13 B. E. Schubert and D. Floreano, *RSC Adv.*, 2013, **3**, 24671–24679.
14 I. De Falco, G. Gerboni, M. Cianchetti and A. Menciassi, *J. Visualized Exp.*, 2015, **105**, e53118.
15 A. Jiang, T. Ranzani, G. Gerboni, L. Lekstutyte, K. Althoefer, P. Dasgupta and T. Nanayakkara, *Soft Rob.*, 2014, **1**, 192–201.
16 V. Wall, R. Deimel and O. Brock, 2015 IEEE International Conference on Robotics and Automation (ICRA), 2015, pp. 252–257.
17 M. R. Jolly, J. D. Carlson, B. C. Muñoz and T. A. Bullions, *J. Intell. Mater. Syst. Struct.*, 1996, **7**, 613–622.
18 M. Moreno, J. Gonzalez-Rico, M. Lopez-Donaire, A. Arias and D. Garcia-Gonzalez, *Composites, Part B*, 2021, **224**, 109148.
19 L. Wang, Y. Yang, Y. Chen, C. Majidi, F. Iida, E. Askounis and Q. Pei, *Mater. Today*, 2018, **21**, 563–576.
20 W. Shan, T. Lu and C. Majidi, *Smart Mater. Struct.*, 2013, **22**, 085005.
21 C. B. Haverkamp, D. Hwang, C. Lee and M. D. Bartlett, *Soft Matter*, 2021, **17**, 1731–1737.
22 M. Manti, V. Cacucciolo and M. Cianchetti, *IEEE Rob. Autom. Mag.*, 2016, **23**, 93–106.
23 J. M. Ginder, M. E. Nichols, L. D. Elie and S. M. Clark, *Smart structures and materials 2000: smart structures and integrated systems*, 2000, pp. 418–425.
24 H. Böse, T. Gerlach and J. Ehrlich, *J. Intell. Mater. Syst. Struct.*, 2021, **32**, 1550–1564.
25 A. K. Bastola and M. Hossain, *Composites, Part B*, 2020, **200**, 108348.
26 V. Ramachandran, M. D. Bartlett, J. Wissman and C. Majidi, *Extreme Mech. Lett.*, 2016, **9**, 282–290.
27 N. Lazarus, C. D. Meyer, S. S. Bedair, G. A. Slipher and I. M. Kierzewski, *ACS Appl. Mater. Interfaces*, 2015, **7**, 10080–10084.

28 L. Cestarollo, S. Smolenski and A. El-Ghazaly, *ACS Appl. Mater. Interfaces*, 2022, **14**, 19002–19011.
29 E. J. Barron III, R. S. Peterson, N. Lazarus and M. D. Bartlett, *ACS Appl. Mater. Interfaces*, 2020, **12**, 50909–50917.
30 K. Hong, M. Choe, S. Kim, H.-M. Lee, B.-J. Kim and S. Park, *Polymers*, 2021, **13**, 2407.
31 M. Ralphs, W. Kong, R. Y. Wang and K. Rykaczewski, *Adv. Mater. Interfaces*, 2019, **6**, 1801857.
32 J. M. Ginder, M. E. Nichols, L. D. Elie and J. L. Tardiff, *Smart Structures and Materials 1999: Smart Materials Technologies*, 1999, pp. 131–138.
33 X.-M. Dong, Y. Miao, C.-R. Liao and W.-M. Chen, *Trans. Nonferrous Met. Soc. China*, 2009, **19**, s611–s615.
34 J. M. Ginder, W. F. Schlotter and M. E. Nichols, *Smart structures and materials 2001: damping and isolation*, 2001, pp. 103–110.
35 J. Bernat, P. Gajewski, R. Kapela, A. Marcinkowska and P. Superczyńska, *Sensors*, 2022, **22**, 2757.
36 D.-S. Choi, T.-H. Kim, S.-H. Lee, C. Pang, J. W. Bae and S.-Y. Kim, *ACS Appl. Mater. Interfaces*, 2020, **12**, 44147–44155.
37 Y. Tsugami, T. Barbié, K. Tadakuma and T. Nishida, 2017 11th Asian control conference (ASCC), 2017, pp. 778–783.
38 J. A. Carpenter, T. B. Eberle, S. Schuerle, A. Rafsanjani and A. R. Studart, *Adv. Intell. Syst.*, 2021, **3**, 2000283.
39 A. B. Croll, N. Hosseini and M. D. Bartlett, *Adv. Mater. Technol.*, 2019, **4**, 1900193.
40 P. Zając, J. Kaleta, D. Lewandowski and A. Gasperowicz, *Smart Mater. Struct.*, 2010, **19**, 045014.
41 S. R. Khimi and K. L. Pickering, *Composites, Part B*, 2015, **83**, 175–183.
42 P. Testa, R. W. Style, J. Cui, C. Donnelly, E. Borisova, P. M. Derlet, E. R. Dufresne and L. J. Heyderman, *Adv. Mater.*, 2019, **31**, 1900561.
43 R. K. Shuib, K. L. Pickering and B. R. Mace, *J. Appl. Polym. Sci.*, 2015, **132**, 41506.
44 B. Dyniewicz, J. M. Bajkowski and C. I. Bajer, *Mech. Syst. Signal Process.*, 2015, **60**, 695–705.
45 I. Bica, E. Anitas and L. Averis, *J. Ind. Eng. Chem.*, 2015, **28**, 86–90.
46 M. Yu, S. Qi, J. Fu, P. Yang and M. Zhu, *Smart Mater. Struct.*, 2015, **24**, 045009.
47 T. Komatsuzaki and Y. Iwata, *Shock Vib.*, 2015, **2015**, 676508.
48 Y. Wang, X. Zhang, J. Oh and K. Chung, *Smart Mater. Struct.*, 2015, **24**, 095006.
49 X. Qiao, X. Lu, X. Gong, T. Yang, K. Sun and X. Chen, *Polym. Test.*, 2015, **47**, 51–58.
50 S. S. Kang, K. Choi, J.-D. Nam and H. J. Choi, *Materials*, 2020, **13**, 4597.
51 M. Yu, P. Yang, J. Fu, S. Liu and S. Qi, *Smart Mater. Struct.*, 2016, **25**, 085046.
52 Y. Tong, X. Dong and M. Qi, *Smart Mater. Struct.*, 2017, **26**, 025023.
53 A. Dobroserdova, M. Schümann, D. Borin, E. Novak, S. Odenbach and S. Kantorovich, *Soft Matter*, 2022, **18**, 496–506.
54 J. Silva, C. Gouveia, G. Dinis, A. Pinto and A. Pereira, *Composites, Part B*, 2022, **243**, 110125.
55 Y. Zhou, S. Jerrams, A. Betts, G. Farrell and L. Chen, *Mater. Des.*, 2015, **67**, 398–404.
56 J. Zhang, Y. Qiao, M. Zhang and P. Zhai, *Smart Mater. Struct.*, 2022, **31**, 095010.
57 A. Boczkowska, S. F. Awietjan and R. Wroblewski, *Smart Mater. Struct.*, 2007, **16**, 1924.
58 A. Bastola, V. Hoang and L. Li, *Mater. Des.*, 2017, **114**, 391–397.
59 M. Ashtiani, S. Hashemabadi and A. Ghaffari, *J. Magn. Magn. Mater.*, 2015, **374**, 716–730.
60 G. Bossis, S. Lacis, A. Meunier and O. Volkova, *J. Magn. Magn. Mater.*, 2002, **252**, 224–228.
61 P. Testa, B. Chappuis, S. Kistler, R. W. Style, L. J. Heyderman and E. R. Dufresne, *Soft Matter*, 2020, **16**, 5806–5811.
62 A. Boczkowska and S. Awietjan, *WIT Trans. Eng. Sci.*, 2011, **72**, 263–274.
63 Z. Varga, G. Filipcsei and M. Zrínyi, *Polymer*, 2006, **47**, 227–233.
64 Y. Li, J. Li, W. Li and H. Du, *Smart Mater. Struct.*, 2014, **23**, 123001.